Atmos. Chem. Phys. Discuss., 14, 8287–8332, 2014
www.atmos-chem-phys-discuss.net/14/8287/2014/
doi:10.5194/acpd-14-8287-2014
© Author(s) 2014. CC Attribution 3.0 License.

Atmospheric Chemistry and Physics Discussions
Open Access

This discussion paper is/has been under review for the journal Atmospheric Chemistry and Physics (ACP). Please refer to the corresponding final paper in ACP if available.

Aircraft observations of five pockets of open cells sampled during VOCALS REx

C. R. Terai, C.S. Bretherton, R. Wood, and G. Painter

Department of Atmospheric Sciences, University of Washington, Seattle, Washington, USA

Received: 14 March 2014 – Accepted: 18 March 2014 – Published: 26 March 2014

Correspondence to: C. R. Terai (terai@atmos.washington.edu)

Published by Copernicus Publications on behalf of the European Geosciences Union.

Abstract

Five pockets of open cells (POCs) are studied using aircraft flights from the VOCALS Regional Experiment, conducted in October and November 2008 over the southeast Pacific Ocean. Satellite imagery from the geostationary satellite GOES-10 is used to distinguish POC areas and measurements from the aircraft flights are used to compare cloud, aerosol, and boundary layer conditions inside and outside of POCs and conditions found across individual POC cases.

POCs are observed in boundary layers with a wide range of inversion heights (1250 to 1600 m) and surface wind speeds (5 to 11 $m\,s^{-1}$) and show no remarkable difference from the observed surface and free tropospheric conditions during the two months of the field campaign. In all cases, compared to the surrounding overcast region the POC boundary layer is more decoupled, supporting both thin stratiform and deeper cumulus clouds. Although cloud-base precipitation rates are higher in the POC than the overcast region in each case, a threshold precipitation rate that differentiates POC precipitation from that in overcast precipitation does not exist. Mean cloud-base precipitation rates in POCs can range from 1.7 to 5.8 $mm\,d^{-1}$ across different POC cases. The occurrence of heavy drizzle (> 0 dBZ) lower in the boundary layer better differentiates POC precipitation from precipitation in the surrounding overcast regions, likely leading to the more active cold pool formation in POCs. Cloud droplet number concentration is at least a factor of eight smaller in the POC clouds, and the ratio of drizzle water to cloud water in POC clouds is over an order of magnitude larger than that in overcast clouds, indicating an enhancement of collision coalescence processes in POC clouds.

Despite large variations in the accumulation-mode aerosol concentrations (65 to 324 cm^{-3}) observed in the surrounding overcast region, the accumulation-mode aerosol concentrations observed in the subcloud layer of all five POCs exhibit a much narrower range (24 to 40 cm^{-3}), and cloud droplet concentrations within the cumulus updrafts originating in this layer reflect this limited variability. Above the POC subcloud layer exists an ultraclean layer with accumulation-mode aerosol concen-

ACPD
14, 8287–8332, 2014

trations < 5 cm^{-3}, demonstrating that in-cloud collision coalescence processes efficiently remove aerosols. It also suggests that the major source of accumulation-mode aerosols, and hence of cloud condensation nuclei in POCs, is the ocean surface, while entrainment of free tropospheric aerosol is weak. The measurements also suggest that at approximately 30 cm^{-3} a balance of surface source and coalescence scavenging sinks of accumulation-mode aerosols maintain the narrow range of observed subcloud aerosol concentrations.

1 Introduction

During most of the year, a large stratocumulus cloud deck covers the southeast Pacific Ocean (SEP), extending westward from the South American continent. Due to a strong albedo and weak greenhouse effect, the stratocumulus exerts a strong cooling effect on the ocean and the atmospheric boundary layer (de Szoeke et al., 2012). The extensive stratocumulus cloud deck is occasionally interrupted by cloud breaks in the form of pockets of open cells, where the lower cloud cover exposes the darker sea surface, effectively lowering the albedo of the area where these features form.

Pockets of open cells (POCs) have previously been defined as regions of open-cell convection completely or largely embedded within a larger region of closed-cell convection (Stevens et al., 2005; Wood et al., 2008). In regions of open-cell convection, patches of descending clear air are ringed by ascending cloudy air, giving it a honeycomb-like pattern when viewed from above. On the other hand, closed-cell convection are characterized by patches of cloudy ascending air that are ringed by clearer descending air, leading to higher albedos (Atkinson and Zhang, 1996; Wood and Hartmann, 2006). Subsequent studies have found, however, that POCs also support thin and extensive stratiform clouds in addition to the honeycomb-like patterns or isolated clusters of deeper cumulus clouds (Wood et al., 2011a) and that horizontal gradients in cloud microphysical properties exist at the transition from closed to open cellular convection, with often dramatic decreases in cloud droplet number concentrations in-

ACPD
14, 8287–8332, 2014

side the POCs (Stevens et al., 2005; Sharon et al., 2006; Wood et al., 2008, 2011a). In this paper, POCs are defined as regions of broken cumuliform convection, possibly overlaid by thin patchy stratocumulus, that (a) are embedded within regions of closed-cell stratocumulus clouds and (b) that also show cloud microphysical changes at the transition, evident in daytime satellite images as an increase in cloud effective radius at the POC edges. This stricter definition of POCs excludes instances of cloud break up that accompany cloud thinning due to increased subsidence and evaporation, and also many cloud breaks at the western edge of stratocumulus cloud decks.

POCs have been observed in satellite imagery (Garay et al., 2004) and in various field experiments (Bretherton et al., 2004; Stevens et al., 2005; Sharon et al., 2006; Wood et al., 2011a). Because the cloud cover is relatively low in POCs, their formation can influence the amount of incident solar radiation that is absorbed at the Earth's surface. Up to 10–15 % of the southeast Pacific region can be covered by POCs during the October and November months of extensive cloud cover (Wood et al., 2008). Although regional models have started to simulate episodic changes in cloud cover and albedo due to synoptic forcing (Abel et al., 2010) and transport of aerosol plumes from coastal pollution sources (Yang et al., 2011; Saide et al., 2012; George et al., 2013), models still do not clearly demonstrate the formation of reduced cloud cover in the form of POCs (Abel et al., 2010; Toniazzo et al., 2011). An exception exists for Mechem and Kogan (2003) who employed a nested 2 km resolution mesoscale model within a larger regional model to form drizzle-induced cloud break up in overcast stratocumulus. The low aerosol concentrations observed within POCs (Petters et al., 2006; Sharon et al., 2006; Wood et al., 2008, 2011a) strongly suggest a mechanism by which aerosols affect clouds and suggest the need to incorporate aerosol–cloud interactions occurring on scales of a few kilometers and smaller to simulate POC formation in models.

Various aspects of the POCs have been convincingly simulated by large-eddy simulations (LES) and high-resolution, cloud-resolving simulations (Wang and Feingold, 2009a, b; Wang et al., 2010; Berner et al., 2011; Kazil et al., 2011; Berner et al., 2013). Several of these studies initialize a region of the model domain with lower cloud droplet

ACPD
14, 8287–8332, 2014

number concentration to initiate POC formation (e.g., Wang and Feingold, 2009a, b; Berner et al., 2011). The simulations point to the importance of cold pools in transforming closed-cell circulation to open-cell circulation (Wang et al., 2010), and indicate horizontal coupling of inversion heights that allows for the coexistence of closed-cell and open-cell clouds within a region of hundreds of kilometers (Berner et al., 2011). Kazil et al. (2011) implemented a more sophisticated model of the sulfur cycle and aerosol processing within an LES and was able to reproduce the observed structure of the aerosol-depleted "ultraclean layer" (as detailed in observations by Wood et al., 2011a) and its potential for supporting spontaneous nucleation of ultrafine aerosol. More recently, Berner et al. (2013) showed that a large-domain cloud-resolving simulation with interactive aerosols can develop long-lived, mutually-supporting regions of open and closed cells existing side by side, suggesting that under some large-scale meteorological and aerosol conditions, the POC-overcast system is a self-maintaining form of mesoscale cloud organization. POC modeling studies have been initialized based on one DYCOMS-II RF02 case (Wang and Feingold, 2009a, b) and one VOCALS case, RF06 (Wang et al., 2010; Berner et al., 2011; Kazil et al., 2011). The boundary layer heights of the two cases range from 800 m (Van Zanten and Stevens, 2005) to 1600 m (Wood et al., 2011a), suggesting diverse environments in which POCs exist. More observational analyses of POCs are therefore necessary to identify the boundary layer properties that are common across different POC cases and those properties that are more variable.

Early observations of POCs were fortuitous because their formation cannot be easily forecast and because they form over remote oceans. The VAMOS Ocean Cloud Atmosphere Land Study Regional Experiment (VOCALS REx), conducted over the southeast Pacific Ocean during October and November of 2008, was the first concerted field campaign for which POCs developing in a larger region were systematically targeted for observational sampling (Wood et al., 2011b; Mechoso et al., 2014). Wood et al. (2011a) provides a detailed analysis of one VOCALS case (RF06) using data from two aircraft. The current study investigates the commonalities and variations across five dif-

ACPD
14, 8287–8332, 2014

ferent VOCALS POC cases, including RF06. We assess our current conceptual model of POC structure and the conditions necessary to form and maintain them. Section 2 gives an overview of the measurements available from the C-130 and describes how POCs are differentiated from the surrounding overcast region using satellite infrared imagery. The following five sections present our results, including the large scale context in which the POCs were observed (Sect. 3) and comparisons of their boundary layer (Sect. 4), cloud and precipitation (Sect. 5), and aerosol (Sect. 6) characteristics with the surrounding overcast regions and too POC-like cases (Sect. 7). A discussion and summary of the results is given in Sect. 8.

2 Data and methods

2.1 Data

During VOCALS REx, six research flights flown by the NSF/NCAR C-130 sampled the atmospheric conditions across transitions from closed-to-open cellular clouds accompanied by clear corresponding changes in cloud microphysics (Wood et al., 2011b). Five of those six research flights are used in this analysis, because the diurnal breakup of the closed-cell stratocumulus made it difficult to distinguish the closed-cell from the open-cell regions during RF14 (15 November). The five remaining research flights examined here are RF06 (28 October), RF07 (31 October), RF08 (2 November), RF09 (4 November), and RF13 (13 November). During VOCALS-REx, if a suspected POC was present within aircraft range when flight plans were made for a given day, the C-130 was directed to sample the POC. The flight strategy consists of sawtooth profile legs from above the inversion to below cloud base, profile legs through the depth of the atmospheric boundary layer, and level flight legs flown ~ 150 m above the surface in the subcloud layer, at cloud base (~ 700 m), at cloud level (~ 1000 m), and above cloud (~ 1500 m). Figure 1 shows a typical flight strategy of POC sampling, followed

ACPD
14, 8287–8332, 2014

by most flights, except for RF06 and RF13, in which an additional subcloud and cloud level flight leg was flown.

For all flight legs, a suite of instruments measured thermodynamic quantities (temperature, water mixing ratio, pressure, etc., described in Wood et al., 2011b) to help characterize the structure of the boundary layer and lower free troposphere. Because the humidity measurements were found to be biased high in previous analyses (Bretherton et al., 2010), the humidity measurements from the Lyman-alpha hygrometer are corrected according to Bretherton et al. (2010). The Wyoming Cloud Radar (WCR), also aboard the C-130, provided radar reflectivity from cloud and precipitation hydrometeors above and below the aircraft. The column maximum reflectivity from the WCR is used to estimate precipitation rates at cloud base inside and outside the POCs using the Z–R relationship from Comstock et al. (2004). From the subcloud flight legs, the cloud fraction, cloud base height, and cloud liquid water path are estimated using the upward pointing Wyoming Cloud Lidar (WCL) and G-band Vapor Radiometer (GVR) (Zuidema et al., 2012), respectively. Sea surface temperatures (SSTs) are remotely sensed by downward viewing Heimann radiometric sensors and corrected by 1 K, to correct a warm bias found by Bretherton et al. (2010).

Concentrations of aerosols of size > 0.1 µm in clear air are obtained from the Passive Cavity Aerosol Spectrometer Probe (PCASP) that measures the size distribution of aerosols with diameter between 0.1 and 3 µm. This size range encompasses most of the accumulation-mode aerosols and is representative of concentrations of cloud condensation nuclei (CCN) at supersaturations typical of those in marine stratocumulus (Martin et al., 1994; Terai et al., 2012). Total aerosol concentrations (CN) for particle diameters > 10 nm were obtained by the 3010 CN Counter (Clarke et al., 2007). Aerosol data are all filtered for possible splashing and shattering events from drizzle drops by removing aerosol data if any of the following conditions are met: liquid water content > 0.04 $g\,m^{-3}$ (as measured by the Gerber PV-100 Probe); drizzle drop concentration > 1 L^{-1} (as measured by the 2DC Probe); a 10 s-forward-lagged, 11 s-moving-window-mean drizzle water content > 10^{-4} $g\,m^{-3}$ (as measured by the 2DC Probe).

ACPD
14, 8287–8332, 2014

Measurements of cloud droplet concentrations (N_d) and mixing ratios (q_c) are obtained from a Cloud Droplet Probe (CDP), which measures drops with radii between 1 and 23.5 µm. Similarly, measurements of drizzle drop concentrations (N_D) and mixing ratios (q_D) are obtained from a 2DC optical array probe for drops with radii larger than 30 µm (Wood et al., 2011b). Unless otherwise stated, all measurements are analyzed at 1 Hz time resolution, corresponding to a spatial resolution of ∼ 100 m. Cloudy air is distinguished from clear air in the cloud-level flight legs when the liquid water mixing ratio from either the Gerber PV-100 Probe or the CDP+2DC exceeded 0.03 g kg^{-1}.

In order to locate the POC boundaries regardless of the time of day, infrared brightness temperature imagery from Channel 4 (centered on 11 µm) of the Geostationary Operational Environmental Satellite imager (GOES-10), obtained roughly every fifteen minutes, is used to locate the flight legs in relation to the POC boundary.

2.2 Differentiating between POC and overcast regions

We divide each relevant flight leg into POC, transition, and overcast (OVC) subsections by visual inspection of the GOES-10 infrared (IR) imagery. This allows us to compare the various boundary layer properties in the POC with those in the overcast region. This approach is similar, but not identical to Wood et al. (2011a) and Berner et al. (2011), who instead used radar reflectivity to distinguish the regions. Figure 2 shows subcloud flight legs from each of the five POC cases overlaid on GOES-10 IR images taken closest to the leg time. The transition region is identified to ensure that POC and overcast sections of the flight leg solely sampled the corresponding cloud types, with its width determined from the sharpness in the transition from overcast to broken clouds along the leg. In the following analysis, we compare the thermodynamic, macrophysical, and microphysical characteristics in the POC region and the overcast region.

ACPD
14, 8287–8332, 2014

3 Large scale context

3.1 Geographical and diurnal context

Four of the POC flights in this study were located at 80° W and just to the north and south of 20° S. The RF13 POC was located slightly to the east at 78° W (see Table 1 and Fig. 2). The region around 20° S and 80° W has been characterized by a combination of aircraft and shipboard measurements made during VOCALS REx (Bretherton et al., 2010; Allen et al., 2011) and shipboard measurements from seven research cruises conducted from 2001 to 2008 (de Szoeke et al., 2012), for which the values are summarized in Tables 2–4. During the October and November months the region was characterized by a median inversion height of ∼ 1240 m (25th–75th percentile range of 1220–1330 m; Bretherton et al., 2010), a diurnal mean cloud thickness of 250 m, corresponding to a mean liquid water path of 81 $g\,m^{-2}$ (de Szoeke et al., 2012), and a mean cloud fraction of 90 % (de Szoeke et al., 2012). Surface mixed layer accumulation-mode aerosol concentrations in the region average approximately 140 cm^{-3}, but with large variations such that the 25th–75th percentile range is 70–220 cm^{-3} (Allen et al., 2011). Because stratocumulus cloud cover and drizzle rates tend to maximize in the early morning hours (Wood et al., 2008; Leon et al., 2008; de Szoeke et al., 2012), and because a goal of VOCALS-REx was to observe the precipitation characteristics in POCs, four of the five POC-sampling research flights were conducted in the early morning hours (Table 1). Large differences in cloud properties between the one POC sampled during mid-day (RF13) and the four POCs sampled during early morning are apparent in the precipitation rate and in-cloud turbulence (Table 3 and Sect. 5.3).

3.2 Synoptic setting

The C-130 VOCALS sampling period of 15 October to 15 November 2008 was characterized as a quiescent period, in which little synoptic activity propagated from the mid-latitudes into the VOCALS region (Toniazzo et al., 2011). During this quiescent pe-

ACPD
14, 8287–8332, 2014

riod, however, POCs contributed substantially to cloud cover variability (Toniazzo et al., 2011). Although no evidence has been found to show that the synoptic waves directly cause the POC features to form or that they help maintain POC features, because mid-latitude storms have the potential of affecting air masses advecting into VOCALS region (George and Wood, 2010), we cannot discount a possible influence from mid-latitude synoptic activity on the formation of POCs.

3.3 Free troposphere

Lower tropospheric stability (LTS) over the subtropical stratocumulus regions is positively correlated with low cloud cover (Klein and Hartmann, 1993; Leon et al., 2008). In Table 2, we compare the LTS, calculated as the potential temperature difference between 700 hPa level and the surface, over the POCs and surrounding overcast region. We find no indication that the VOCALS POCs formed under remarkably high or low LTS conditions. Because the aircraft did not fly many profiles up to 700 hPa (~ 3100 m), the same 700 hPa potential temperatures are used to calculate LTS in POCs and overcast regions in Table 2. The surface potential temperatures are the mean potential temperature from the subcloud legs in each region. Because surface potential temperatures did not vary by much between separate POC cases (287–289 K), variations in LTS between cases are largely due to differences in the 700 hPa temperatures.

Stevens et al. (2005) observed a moister free troposphere (FT) above a northeast Pacific POC, which led to the hypothesis that POCs formed under regions with moister FT. Wood et al. (2008), however, found no evidence in the southeast Pacific that POCs formed preferentially in regions with a moister FT. Likewise, if we compare the water vapor mixing ratio (q_v) from the above-cloud flight legs flown over the POC and overcast region, then we find that q_v is not consistently higher above the VOCALS POCs (Table 2).

ACPD
14, 8287–8332, 2014

4 Boundary layer structure

4.1 Air–sea temperature difference

Air-sea temperature differences and wind speeds determine the temperature flux at the surface. Except for RF13, the SSTs are slightly lower in the POC than in the overcast region (Table 2). However, the apparent SST decrease in the POC might be a sampling artifact, because the intervening water vapor between the aircraft and sea surface can affect radiometric SST estimates from the pyrometer (Stevens et al., 2005). Given that the subcloud temperature in the POC is approximately 1 K lower and the water vapor mixing ratio is 1 $g\,kg^{-1}$ higher, we would expect SSTs retrieved in the POC region to be biased lower than SSTs retrieved in the overcast region. Despite this potential low bias of the POC SSTs, the estimated air–sea temperature difference inside the POC is larger than in the overcast region (Table 2). The cooler surface air temperatures in the POC, likely a result of cold pool formation, increase the air–sea temperature difference in the POC.

Relative changes in wind speed across the POC-overcast transition are small (Table 2). Therefore, any systematic changes in the surface sensible and latent heat fluxes are likely due to air–sea temperature and moisture differences in the POC. Across different POCs, a large range in surface-level horizontal wind speeds was measured (Table 2), which indicates that the maintenance of POCs does not require stronger or weaker winds.

4.2 Inversion height and structure

The inversion height is a critical parameter in marine boundary layer (MBL) evolution which caps the cloud top height and affects the likelihood of boundary layer decoupling (Jones et al., 2011). The inversion base height ($z_{i,\,base}$) is estimated from the profile legs as the height of the coldest temperature in the lower troposphere (Jones et al., 2011; Wood et al., 2011a). The $z_{i,\,base}$ of the observed POCs and the surrounding

ACPD
14, 8287–8332, 2014

clouds range from 1250 to 1650 m (Table 2), which is on the higher end of the range of $z_{i,\,base}$ observed at 80° W during all the VOCALS-REx flights (Bretherton et al., 2010), but there is no indication that POCs only form in deeper boundary layers. If we compare the POC with the surrounding overcast region, the inversion base height is 25 to 100 m lower in the POC than in the overcast region in RF06, RF07, RF08, and RF09, but 50 m higher for RF13, the one POC sampled during the daytime. Inadequate sampling precludes attributing this difference to the diurnal cycle. The $z_{i,\,base}$ observed in the VOCALS POCs are substantially deeper than the 700–800 m inversion base heights of POCs observed previously over the northeast Pacific (see Table 2; Van Zanten and Stevens, 2005; Sharon et al., 2006). We conclude that POCs can be produced in boundary layers with a range of inversion heights.

The strength of the inversion determines how easily free tropospheric air can be entrained into the MBL. We compare the inversion structure over the POC and overcast region in Fig. 3. A mean profile for the overcast and POC region is constructed for each case from averaging the potential temperature from the profiles in 25 m height bins. To compare results from different POC cases, the mean inversion height (z_i) from each POC and overcast case found in Table 2 is subtracted from each profile. Rather than using $z_{i,\,base}$ for this purpose (which would align the bottom of the gradient regions in the profiles), we define the z_i in each flight profile to correspond to the maximum of the 5 s-running-mean of $d\theta/dz$ and subtract the mean of those heights from each averaged profile. Table 2 gives this mean z_i for the POC and overcast (OVC) regions of each flight; for the four nocturnal flights, the mean z_i is quite similar in the POC and OVC regions, even though $z_{i,\,base}$ is lower in the POC. Figure 3 shows that the inversion is typically sharper in the OVC region than in the POC. This is expected given how radiative cooling from thick overcast clouds helps to sharpen the inversion. However, the inversion structure also differs from case to case. For example, the inversion in the overcast profile from RF09 is especially hard to identify. This is partly a result of averaging six different overcast profiles into one, but visual inspection shows that the

ACPD
14, 8287–8332, 2014

inversions in individual profiles from the overcast region of RF09 are also less sharp than in other cases.

4.3 Decoupling

The degree to which the boundary layer is decoupled can be quantified by taking the difference (Δz) between the cloud base height and the lifting condensation level (LCL) from the subcloud flight legs (Jones et al., 2011). Defined this way, the decoupling gives an indication of the relative timescales between boundary layer mixing and processes that act to stabilize the boundary layer. From Table 3, we see that for all cases, the POC has a significantly (150–350 m) lower LCL. In the nocturnal cases, the Δz is larger (indicating stronger decoupling) in the POC than the surrounding OVC region. In the one daytime flight (RF13), the OVC is more decoupled, consistent with observational and large eddy simulation studies that find that solar insolation strongly decouples the daytime overcast boundary layer (Turton and Nicholls, 1987; Bretherton et al., 2004; Caldwell and Bretherton, 2009). Although Wood et al. (2011a) noted that the OVC region surrounding the RF06 POC was well-mixed ($\Delta z = 86$ m), we find that this feature is not shared across the other POC cases.

The stronger decoupling in POCs is likely a manifestation of strong drizzle evaporation in the subcloud layer that leads to the stabilization and decoupling of the lower boundary layer. This traps surface fluxes in the lower levels of the boundary layer and leads to lower LCL. LES studies have shown that the increased stability from subcloud drizzle evaporation enhances the transition from closed to open cellular convection (Savic-Jovcic and Stevens, 2008) and that cold pools help to organize cumulus cloud convection (Wang et al., 2010; Berner et al., 2011). It should however be noted that cold pools are not exclusive to POCs, but are also observed under non-POC forming overcast stratocumulus, and hence do not serve as a sufficient condition for POC formation (Terai and Wood, 2013).

ACPD
14, 8287–8332, 2014

4.4 Vertical wind variance ($\overline{w'^2}$)

Counteracting the stabilization of the boundary layer, the radiative cooling at cloud top drives turbulence and enhances the mixing between the cloud layer and underlying surface mixed layer. The strength of the turbulence can be quantified by the vertical velocity variance ($\overline{w'^2}$) measured within cloud-layer legs. Corroborating Wood et al. (2011a), we find that $\overline{w'^2}$ is lower in the POC across all cases (Table 3). The very low $\overline{w'^2}$ values in both POC and OVC regions in the RF13 case sampled during mid-day are probably due to absorption of solar radiation, which reduces the net cloud-layer radiative cooling that helps drive turbulence. It is illuminating to see local variations in $\overline{w'^2}$ over the course of a flight leg, which we calculate based on a 21 s (~2 km) moving window, which acts as a crude high-pass filter to isolate turbulent motions from mesoscale fluctuations. In Fig. 4, measurements from the cloud-level flight leg of the RF08 POC are shown to illustrate the observed changes in cloud, drizzle, and vertical wind speed across the POC-to-OVC transition. Figure 4b shows that $\overline{w'^2}$ is intermittent in the POC. Long stretches of very low $\overline{w'^2}$ are interrupted by short bursts of elevated $\overline{w'^2}$, which are associated with cumulus clouds. Although there are fluctuations in $\overline{w'^2}$ in the overcast region, the values are generally high. Cloud level $\overline{w'^2}$ also gives an indication of how much turbulence is available to entrain air from the FT. The much lower values of cloud-layer $\overline{w'^2}$ within POC regions compared to surrounding overcast regions with similar inversion temperature jumps suggest that the entrainment rates over the POCs are much smaller than in the surrounding overcast regions, as found with LES (Berner et al., 2011).

ACPD
14, 8287–8332, 2014

5 Clouds and precipitation

5.1 Cloud macrophysics

A defining difference between the POC and overcast regions in a satellite image is the difference in cloud fraction. For cloud fraction estimates we use the upward-pointing Wyoming Cloud Lidar to detect overlying cloud during the C-130 subcloud flight legs. Cloud fraction in overcast regions are nearly 100 %, while on average, the POC regions have more variable cloud fraction between 56 % and 83 % (Table 3). The all-sky mean LWP can be higher or lower in the POC than in the OVC region, but the relative standard deviation of LWP (the ratio of the standard deviation of LWP to its mean, both given in Table 3), tends to be larger in the POC. This, together with enhanced decoupling, is an indicator of more cumulus-like convection within the POC (Jones et al., 2011).

These differences in cloud structures also manifest themselves in the precipitation rates. The mean precipitation rates are higher in the POCs than in the surrounding OVC regions (Table 3). POC radar reflectivities are also more broadly distributed. The column maximum radar reflectivity (Z_{max}) is plotted against the fraction of columns with reflectivity greater than that value in Fig. 5a. The broader distribution in the POC is evident from the shallower slope of the POC cumulative distribution, compared to the OVC. In particular, there is a much larger fractional coverage of strong drizzle > 10 dBZ for all POC cases. This contrast is consistent with statistics of the distribution of reflectivities within open and closed cell stratocumulus observed previously over the SEP with shipboard cloud radar (Comstock et al., 2007) and over the global oceans with CloudSat (Muhlbauer et al., 2014).

Terai and Wood (2013) found that precipitation at lower elevations is a better indicator of cold pool formation than the occurrence of precipitation at cloud base (where the column maximum reflectivity is observed). Similarly, by examining the reflectivity at 250 m (Z_{250}) in Fig. 5b, instead of the column maximum (Z_{max}), we find that reflectivities greater than 0 dBZ occur on average 10 % of the time in POCs compared to only ~ 1.5 % of the time in the OVC region. Among the different precipitation characteristics,

ACPD
14, 8287–8332, 2014

this best differentiates the POC precipitation from the OVC precipitation. The reflectivities at 250 m are likely influenced by the amount of subcloud evaporation between the cloud base and 250 m. Therefore, the higher occurrence of > 0 dBZ precipitation at 250 m in the POC may reflect lower cloud base heights in the POCs rather than a difference in the drizzle drop size distributions.

The macrophysical signatures of the cloud and precipitation properties in POCs all point to more cumuliform convection and correspondingly patchier and heavier precipitation within the POC than the surrounding overcast region.

5.2 Cloud microphysics

We now consider the cloud microphysical properties in the POCs. Consistent with previous POC observations (Petters et al., 2006; Sharon et al., 2006; Van Zanten and Stevens, 2005; Wood et al., 2011a), all five of the POC cases examined here show cloud droplet number concentrations (N_d) decrease by more than a factor of eight from the OVC region (Table 4). Whereas the mean cloud-layer N_d inside the POCs has a range between 4 and 13 cm^{-3} across cases, the N_d in the surrounding OVC region range from 52 to 207 cm^{-3}, further showing that POCs can persist when surrounded by a wide range of microphysical environments. In the surrounding OVC, the case-to-case variations in N_d are highly correlated ($r = 0.98$) with the variations in subcloud PCASP aerosol concentrations (N_a). In the POCs, the relative changes in N_d is much more spatially variable than in OVC clouds, and N_d is at least a factor of three lower than the subcloud N_a. As we discuss below (Sect. 5.3), this is due to dramatically lower N_d in "quiescent" stratocumulus clouds than in the "active" cumulus clouds that bring up the subcloud-layer aerosol. Despite this, the mean subcloud N_a is correlated to N_d in the POCs ($r = 0.76$).

The horizontal-mean cloud water mixing ratio (q_c) drops drastically inside the POCs (Table 4), due in part to a lower cloud fraction. In contrast, the horizontal-mean drizzle water mixing ratio (q_D) at least doubles inside the POCs, such that in all five POC cases

ACPD
14, 8287–8332, 2014

the mass of water in the drizzle mode is larger than that in the cloud mode; remarkably, the q_D/q_c ratio is at least twenty-fold larger in the five POCs than in the OVC regions. The increase in the estimated precipitation rate from the surrounding OVC region to the POC is not as large as that in q_D.

This apparent discrepancy is explained by the distinct size distribution of cloud and drizzle drops in the POC (Fig. 6). If we examine the cloud and drizzle drop size distributions measured by the CDP and 2DC in Fig. 6, we note a large increase in the drizzle drop concentrations in the POCs. However, since these are the smallest of drizzle drops, while they may contribute to a substantial proportion of the drizzle mass, they do not contribute strongly to the precipitation rate. The increase in the number of large cloud and small drizzle drops is curious and may be related to the very low N_d and different cloud types in POCs.

5.3 Active vs. quiescent clouds

A closer examination of the clouds found in POCs reveals two general types of clouds: thinner, stratiform, quiescent clouds and cumulus-like active clouds (Wood et al., 2011a). We use a $\overline{w'^2}$ threshold of $0.1\,m^2\,s^{-2}$ as a means of distinguishing between the quiescent and active clouds inside the POC, except for the daytime case RF13, where the overall cloud-level vertical wind variance is low and hence where a threshold of $0.03\,m^2\,s^{-2}$ is used. In the RF08 example (Fig. 4), one can see lower N_d, lower vertical velocities, and consistently elevated drizzle drop number concentrations (N_D) in the quiescent clouds than in the active clouds. Table 5 quantifies and summarizes differences between the active and quiescent clouds in the POC regions, averaged for each of the five cases. Note that unlike Table 4, all of the listed variables are only averaged over cloudy portions of the flight leg. Although there are uncertainties in taking area estimates from one or two cloud-level flight legs, we find that across all POC cases, the quiescent clouds make up most of the observed clouds in the POCs. The cloud droplet number concentration N_d is consistently lower within the quiescent clouds than

ACPD
14, 8287–8332, 2014

in the active clouds, the latter having mean N_d on the order of 15 cm^{-3}. RF07 is an apparent exception, but active clouds were rarely sampled on this flight, with only 2 km of the flight leg sampling active clouds. The ratio between q_c and q_D differ between the two regions, much like the change in ratio between overcast and POC clouds; in active clouds, q_c and q_D are comparable, whereas in quiescent clouds, q_D is far greater. Nonetheless, it is important to note that the q_D in both active and quiescent clouds of the POC is far greater than in the overcast clouds. The high q_D is likely to increase the accretion and self-collection rates in POCs. Table 5 shows, however, that in each POC case higher q_D in quiescent clouds does not always translate to higher precipitation rates, which are estimated from the in situ 2DC-measured drizzle size distribution averaged over the appropriate cloud type. As in the POC-overcast comparison, this discrepancy exists because much of the drizzle mass difference resides at the smaller sizes, which have a smaller influence on precipitation rate.

6 Aerosol

6.1 Accumulation-mode aerosol

Some of the macrophysical difference between the overcast and POC cloud characteristics are attributable to differences in inversion structure and LCL height. Many of the microphysical differences, such as differences in N_d, are attributable to the low accumulation-mode aerosol concentrations (N_a) in POCs. The POC subcloud-layer N_a of ~ 30 cm^{-3} (Table 4), as measured by the PCASP, are much lower than the typical 25–75th percentile range of 70–220 cm^{-3} (Allen et al., 2011) in the 80° W region during the VOCALS-REx time period. N_a in the surrounding overcast regions range between 64 and 330 cm^{-3} across the five cases, similar to the REx-mean distribution near 80° W, and are well-correlated with N_d (Table 4). The cases (e.g., RF08) with higher N_a in the overcast region are related to hook features associated with localized offshore aerosol transport in the free-troposphere and boundary layer, described

ACPD
14, 8287–8332, 2014

by George et al. (2013). The subcloud N_a in the POC is uncorrelated with N_a in the surrounding overcast and shows remarkable small variation (24–40 cm^{-3}) across the five POC cases. If we extend the comparison to other previously observed POC cases (Sharon et al., 2006; Petters et al., 2006; Wood et al., 2008), the similarity in subcloud N_a still holds (Table 4). Spatially, across the overcast-to-POC transition, subcloud N_a gradually decreases over tens of kilometers across the transition (Fig. 2), whose gradients across the transition vary from case to case. Even within the POC, Fig. 2 and Table 4 show that subcloud N_a can spatially vary by more than 25 %.

Whereas we have mostly examined data collected during the level flight legs to examine horizontal gradients in N_a, we use both the profiles and level flight legs to examine the vertical distribution of N_a (Fig. 7). In the RF06 case, Wood et al. (2011a) noted a layer of ultraclean air in the POC region where mean PCASP aerosol concentrations are considerably lower than 10 cm^{-3}. We find that an ultraclean layer exists in all of the other POC cases examined during VOCALS. The ultraclean layers typically extend from roughly the stratocumulus cloud base height to the inversion base, with a broad range of thicknesses (from 200 m for RF06 to 700 m for RF07). The concentrations in the ultraclean layer also vary from case to case, ranging from the very clean RF09 case, where a 400 m layer with concentrations < 1 cm^{-3} was observed, to the more polluted RF08 case, where concentrations mostly hovered around 5 cm^{-3} and those concentrations < 1 cm^{-3} were rarely observed. Concerning the structure of the ultraclean layer, with the exception of RF08, the vertical gradient in aerosol concentration is sharper at the inversion compared to the more gradual change from relatively well-mixed subcloud layer to the ultraclean layer.

6.2 Aitken-mode aerosol

Whereas N_a is much lower in the POC at all heights, the same is not true for concentrations of smaller aerosol particles. Past shipboard measurements (Kollias et al., 2004; Petters et al., 2006; Tomlinson et al., 2007; Wood et al., 2008) reported an increase in the number of Aitken-mode aerosols in the very clean regions of the POCs, suggesting

ACPD
14, 8287–8332, 2014

that the low aerosol concentrations in the POC allow for the nucleation of Aitken-mode aerosols. Their growth to accumulation-mode sizes may potentially provide a source of CCN in the POC (Kazil et al., 2011). The Aitken-mode aerosol concentration is estimated from our C-130 observations as the difference between total aerosol concentrations for particles with diameter > 10 nm (CN) and those from the PCASP (> 100 nm). From our observations of the five POC cases, no clear picture of enhanced or depleted Aitken-mode aerosols emerges. Subcloud Aitken-mode aerosol concentrations in the POC only increase for three of the five cases (RF06, RF08, and RF09; Table 4), and their concentrations do not correlate with subcloud N_a. We also find that except for the daytime RF13 flight, the concentration of Aitken-mode aerosols decreases in the ultraclean layer, where we expect the highest nucleation rates due to low aerosol surface concentrations. It must be noted that four of the POCs were sampled during the night, when photochemical production of nucleation mode precursor gases is absent. What we can say is that unlike the accumulation-mode aerosols, which have a large sink in incloud coalescence scavenging across all POCs, which defines their vertical horizontal structure, the Aitken-mode aerosols appear to be modulated by a variety of processes that are not as well constrained across different POC cases.

6.3 Accumulation-mode aerosol budget in POCs

Although we should entertain the possibility that the relatively small variation between cases in POC subcloud N_a is coincidental, it certainly warrants attention. The similarity across different POCs indicates that the source and sink balance of accumulation-mode aerosols somehow gives rise to relatively constant concentrations. The small spread between cases is surprising given that the observations are strongly suggestive of a surface source of aerosols and that mean surface wind speeds vary between 5 and 11 $m\,s^{-1}$ between cases. Surface aerosol fluxes from sea-salt flux parameterizations are strong functions of wind speed (e.g., de Leeuw et al., 2011). If we assume that the primary source of aerosols in the POC is indeed the ocean surface, then a steady-state

ACPD
14, 8287–8332, 2014

CCN concentration in the POC subcloud layer (N_s) can be estimated with the equation:

$$N_s = N_+ + \frac{F}{M_{Cu}}, \tag{1}$$

where N_+ is the CCN concentration just above the subcloud layer, F is the surface source of CCN-sized aerosols, and M_{Cu} is the entrained mass flux into the subcloud layer from above, that keeps the surface layer partially coupled to the cloud layer in the POC. This must equal the cumulus mass flux out of the subcloud layer. In other words, the surface flux of CCN at the surface is balanced by the mixing of CCN-depleted air into the top of the surface layer.

We may obtain estimates of N_+, F, and M_{Cu} to verify whether this balance equation applies to the observed POC cases. N_+ is estimated as the mean PCASP aerosol concentration from the below cloud flight legs. F is estimated using the sea salt flux parameterization from Clarke et al. (2006), integrated over the size distribution of PCASP-size aerosols. The 10 m mean wind speed (u_{10}) that is needed for the calculation is estimated from the mean wind speed measured in the subcloud legs and assuming a log-wind profile with a surface roughness of 1.86×10^{-4} m (Wood et al., 2011a). Because the parameterized aerosol flux has a dependence of $u_{10}^{3.41}$, an order of magnitude difference in fluxes exists between the low and high wind conditions (see Table 6). The cumulus mass flux (M_{Cu}) can be estimated from examining the water balance at the top of the subcloud layer. If we assume that the upward moisture flux in the cumulus clouds is balanced by precipitation rates, then M_{Cu} can be estimated as

$$M_{Cu} = \frac{R_{500}}{\Delta q}\rho, \tag{2}$$

where R_{500} is the precipitation rate at 500 m, Δq is the moisture difference between cloudy and clear parcels at the top of the subcloud layer, and ρ is the air density, which we assume to be 1 kg m^{-3}. The precipitation rate at 500 m is chosen, because this is the approximate height of the LCL (Table 3), which typically coincides with the

ACPD
14, 8287–8332, 2014

height of the top of the subcloud layer. The estimated cumulus mass fluxes, reported in Table 6, range between 1.0 and 2.8 $\mathrm{cm\,s^{-1}}$. Except in RF09, the estimated F/M_{Cu} is much smaller than the observed $N_{\mathrm{s}} - N_{+}$, inconsistent with the balance (Eq. 1). There are several possible reasons for this discrepancy. First, determining an appropriate N_{+} is made difficult by the vertical gradient in N_{a} at the top of the subcloud layer, as evident in Fig. 7. Rather than decreasing abruptly at the top of the subcloud layer, N_{a} gradually decreases upward into the cloud layer. Second, we have neglected any other sources of CCN-sized aerosols, such as the growth of Aitken-mode aerosols to accumulation-mode sized particles. Third, other budget terms such as losses from precipitation scavenging of aerosols in the subcloud layer could be significant. What we can say from the values in Table 6 is that F/M_{Cu} can easily vary by more than a factor of four, and their variations do not correlate with N_{s} or $N_{\mathrm{s}} - N_{+}$. We are therefore left without an explanation to why the subcloud N_{a} in POC varies so weakly across different POC cases.

7 Non-POC cases

Two cases of cloud breaks which may appear as contenders for POCs, but which are excluded from our definition of POCs, are examined here. The first case of cloud break-up sampled during RF02 (18 October) and shown in Fig. 8a was sampled to the south of a hook-like cloud feature of enhanced N_{d} from the transport and entrainment from the free troposphere of anthropogenic aerosols (George et al., 2013). Despite the break in the cloud to the south of the hook feature, we do not identify this feature as a POC, because it lacks the microphysical change (a substantial increase in effective radius at its edges) that we associate with POCs. In situ observations show that instead of a decrease in accumulation-mode aerosols, there is a subsequent increase in subcloud N_{a} from ~ 200 to $\sim 300\,\mathrm{cm^{-3}}$ to the south. Likewise, the N_{d} increases from ~ 100 to $\sim 200\,\mathrm{cm^{-3}}$ (not shown). From the C-130 observation alone, however, we cannot determine the reason for the cloud break-up to the south. We do find that the inversion

ACPD
14, 8287–8332, 2014

at approximately 1000 m around 83° W is anomalously low, and the decrease in cloud cell size to the south in the satellite visible imagery hints at a lowering of the inversion height to the south that might mean a lowering of cloud top heights to the south.

The second case (Fig. 8b) corresponds to western edge of the stratocumulus cloud deck observed during RF04 (23 October), where large drizzle rates were observed. High radar reflectivities (> 10 dBZ), representing heavy drizzle, cold pool formation, and an increase in cloud effective radius towards the edge of the cloud deck were observed in daytime satellite retrievals of this case, but no open cellular convection was observed beyond the edge of the overcast clouds, excluding this case from our definition of POCs. We also do not observe a decrease in N_a to the west of the break up, although a decrease of aerosols in the clear region is not part of the definition of POCs in this study. This suggests that higher precipitation rates at the edges of overcast clouds do not always indicate that the strong aerosol–cloud–precipitation interactions that we observe in POCs are the cause for the break-up in the clouds.

8 Discussion and conclusions

Five pockets of open cells (POCs) sampled during VOCALS-REx by the NSF/NCAR C-130 are comprehensively compared with their surrounding overcast regions. Free tropospheric water vapor and temperature, sea surface temperatures, inversion height, and near-surface winds were not found to differ appreciably in the POCs compared with the surrounding overcast stratocumulus areas, and are not very different from the REx-mean conditions in the sampled regions. This latter fact indicates that POCs can be maintained under typical large-scale meteorological conditions found over the Southeast Pacific.

A consistent feature of POCs is the presence of heavy drizzle rates (> 10 dBZ) and associated cold pools, which are largely absent in the surrounding overcast regions. All five of the observed POCs also contain both active, cumuliform and quiescent, stratiform clouds. Active clouds associated with cumulus-like convection, make up a

ACPD
14, 8287–8332, 2014

smaller proportion of the cloud cover (CF < 25 %) in the POC and have larger cloud droplet number concentrations (N_d) and larger cloud water mixing ratios (q_c). Although collision-coalescence rates are expected to be high in the active clouds, their comparatively high N_d (20 cm^{-3}) suggests that active clouds loft relatively aerosol-rich subcloud-layer air to the cloud layer and detrain some of this aerosol into surrounding quiescent clouds, which cover more of the POCs and are characterized by very low N_d (< 10 cm^{-3}) and high drizzle water mixing ratio (q_D). We cannot determine from these observations whether quiescent clouds are spatial extensions of active cells, as in the trailing stratiform region of larger mesoscale convective systems, are remnants of decaying active clouds, or are formed in situ. Snapshots of POC cloud fields from LES studies of Berner et al. (2011) and Kazil et al. (2011) suggest that quiescent clouds are spatial extensions of active cumulus clouds, but a closer examination of the time evolution of quiescent clouds will be necessary to resolve this issue.

The efficiency of the in-cloud coalescence scavenging in cleaning out accumulation-mode aerosols in POCs is most evident in the apparently omnipresent ultraclean layer observed across all five POCs. The presence of the ultraclean layer, combined with the low values of vertical velocity variance in the cloud layer within the POC and increased aerosol concentrations at lower altitudes, also strongly suggests that the surface source of accumulation-mode aerosols, and hence of cloud condensation nuclei, is more important than a free tropospheric source. In addition, we find that the spread of mean subcloud-layer accumulation-mode aerosol concentration (N_a) in the POCs is remarkably narrow, with a mean value (~ 30 cm^{-3}) that is close to values found in previously studied cases from other locations and times (Sharon et al., 2006; Petters et al., 2006; Wood et al., 2008). This mean value appears to be insensitive to N_a in the surrounding overcast region, suggesting that the factors controlling the aerosol budget in the POC are independent of those in the surrounding overcast.

The factors that determine the N_a budget in the POC subcloud layer in the simple aerosol budget of Eq. (1) are quantified in Table 6. We find that our simple budget calculation does not shed light on explaining the narrow range of observed subcloud

ACPD
14, 8287–8332, 2014

N_a in POCs. Instead it leaves us with a puzzle as to how the narrow range of N_a exists when the surface source of aerosols can differ by more than an order of magnitude. Because high resolution cloud resolving model studies with interactive aerosols also show similar accumulation-mode aerosol concentrations in the subcloud layer (Kazil et al., 2011; Berner et al., 2013), further modeling studies with variable surface source functions may help shed light on whether there is indeed a physical explanation for the similarity.

Finally it is important to state that while this study informs the mechanisms involved in POC maintenance, it does not inform the mechanisms by which POCs form. Previous modeling studies have looked at the transition from closed-cell to open cell convection mediated by cold pool formation (Wang et al., 2010), cloud-aerosol interactions (Kazil et al., 2011), or high liquid water path (Wang et al., 2010; Berner et al., 2013). Observational studies have noted the possible role of gravity waves (Allen et al., 2013) or larger cloud droplet sizes (Wood et al., 2008) in POC formation, but widespread observational data is still lacking, largely because POCs preferentially form overnight (Wood et al., 2008). A concerted effort to combine satellite retrievals and regional models will likely be necessary to pin down the key factors that contribute to POC formation; in a future paper, we will present a satellite-based study of the evolution of the five VOCALS-REx POC cases prior to the in situ aircraft observations.

Acknowledgements. Funding for this work was provided by NSF grants ATM-0745702 and AGS-1242639. The authors thank the scientists, staff, ground-crew and aircrew at the NCAR Research Aviation Facility, and the C-130 scientists who were instrumental in the collection of the data analyzed here. The C-130 data were provided by NCAR/EOL under sponsorship of the National Science Foundation. http://data.eol.ucar.edu/.

References

Atkinson, B. and Zhang, J. W.: Mesoscale shallow convection in the atmosphere, Rev. Geophys., 34, 403–431, doi:10.1029/96RG02623, 1996. 8289

ACPD
14, 8287–8332, 2014

Abel, S. J., Walters, D. N., and Allen, G.: Evaluation of stratocumulus cloud prediction in the Met Office forecast model during VOCALS-REx, Atmos. Chem. Phys., 10, 10541–10559, doi:10.5194/acp-10-10541-2010, 2010. 8290

Allen, G., Coe, H., Clarke, A., Bretherton, C., Wood, R., Abel, S. J., Barrett, P., Brown, P., George, R., Freitag, S., McNaughton, C., Howell, S., Shank, L., Kapustin, V., Brekhovskikh, V., Kleinman, L., Lee, Y.-N., Springston, S., Toniazzo, T., Krejci, R., Fochesatto, J., Shaw, G., Krecl, P., Brooks, B., McMeeking, G., Bower, K. N., Williams, P. I., Crosier, J., Crawford, I., Connolly, P., Allan, J. D., Covert, D., Bandy, A. R., Russell, L. M., Trembath, J., Bart, M., McQuaid, J. B., Wang, J., and Chand, D.: South East Pacific atmospheric composition and variability sampled along 20° S during VOCALS-REx, Atmos. Chem. Phys., 11, 5237–5262, doi:10.5194/acp-11-5237-2011, 2011. 8295, 8304, 8321

Allen, G., Vaughan, G., Toniazzo, T., Coe, H., Connolly, P., Yuter, S. E., Burleyson, C. D., Minnis, P., and Ayers, J. K.: Gravity-wave-induced perturbations in marine stratocumulus. Q. J. Roy. Meteor. Soc., 139, 32–45, doi:10.1002/qj.1952, 2013. 8311

Berner, A. H., Bretherton, C. S., and Wood, R.: Large-eddy simulation of mesoscale dynamics and entrainment around a pocket of open cells observed in VOCALS-REx RF06, Atmos. Chem. Phys., 11, 10525–10540, doi:10.5194/acp-11-10525-2011, 2011. 8290, 8291, 8294, 8299, 8300, 8310

Berner, A. H., Bretherton, C. S., Wood, R., and Muhlbauer, A.: Marine boundary layer cloud regimes and POC formation in a CRM coupled to a bulk aerosol scheme, Atmos. Chem. Phys., 13, 12549–12572, doi:10.5194/acp-13-12549-2013, 2013. 8290, 8291, 8311

Bretherton, C. S., Uttal, T., Fairall, C. W., Yuter, S. E.,Weller, R. A., Baumgardner, D., Comstock, K., and Wood, R.: The EPIC 2001stratocumulus study, B. Am. Meteorol. Soc., 85, 967–977, doi:10.1175/BAMS-85-7-967, 2004. 8290, 8299

Bretherton, C. S., Wood, R., George, R. C., Leon, D., Allen, G., and Zheng, X.: Southeast Pacific stratocumulus clouds, precipitation and boundary layer structure sampled along 20° S during VOCALS-REx, Atmos. Chem. Phys., 10, 10639–10654, doi:10.5194/acp-10-10639-2010, 2010. 8293, 8295, 8298, 8319

Caldwell, P., and Bretherton, C. S.: Large Eddy simulation of the diurnal cycle in Southeast Pacific stratocumulus, J. Atmos. Sci., 66, 432–449, doi:10.1175/2008JAS2785.1, 2009. 8299

Clarke, A. D., Owens, S. R., and Zhou, J.: An ultrafine sea-salt flux from breaking waves: implications for cloud condensation nuclei in remote marine atmosphere, J. Geophys. Res., 111, 06202, doi:10.1029/2005JD006565, 2006. 8307, 8323

Clarke, A., McNaughton, C., Kapustin, V., Shinozuka, Y., Howell, S., Dibb, J., Zhou, J., Anderson, B., Brekhovskikh, V., Turner, H., and Pinkerton, M.: Biomass burning and pollution aerosol over North America: organic components and their influence on spectral optical properties and humidification response, J. Geophys. Res., 112, D12S18, doi:10.1029/2006JD007777, 2007. 8293

Comstock, K. K., Wood, R., Yuter, S. E., and Bretherton, C. S.: Reflectivity and rain rate in and below drizzling stratocumulus, Q. J. Roy. Meteor. Soc., 130, 2891–2918, doi:10.1256/qj.03.187, 2004. 8293, 8323

Comstock, K. K., Yuter, S. E., Wood, R., and Bretherton, C. S.: The three-dimensional structure and kinematics of drizzling stratocumulus, Mon. Weather Rev., 135, 3767–3784, doi:10.1175/2007MWR1944.1, 2007. 8301

de Leeuw, G., Andreas, E. L., Anguelova, M. D., Fairall, C. W., Lewis, E. R., O'Dowd, C., Schulz, M., and Schwartz, S. E.: Production flux of sea spray aerosol, Rev. Geophys., 49, RG2001, doi:10.1029/2010RG000349, 2011. 8306

de Szoeke, S. P., Yuter, S., Mechem, D., Fairall, C. W., Burleyson, C. D., and Zuidema, P.: Observations of stratocumulus clouds and their effect on the Eastern Pacific surface heat budget along 20° S, J. Climate, 25, 8542–8567, doi:10.1175/JCLI-D-11-00618.1, 2012. 8289, 8295, 8320

Garay, M. J., Davies, R., Averill, C., and Westphal, J. A.: Actinoform clouds: overlooked examples of cloud self-organization at the mesoscale, B. Am. Meteorol. Soc., 85, 1585–1594, doi:10.1175/BAMS-85-10-1585, 2004. 8290

George, R. C. and Wood, R.: Subseasonal variability of low cloud radiative properties over the southeast Pacific Ocean, Atmos. Chem. Phys., 10, 4047–4063, doi:10.5194/acp-10-4047-2010, 2010. 8296

George, R. C., Wood, R., Bretherton, C. S., and Painter, G.: Development and impact of hooks of high droplet concentration on remote southeast Pacific stratocumulus, Atmos. Chem. Phys., 13, 6305–6328, doi:10.5194/acp-13-6305-2013, 2013. 8290, 8305, 8308

Jones, C. R., Bretherton, C. S., and Leon, D.: Coupled vs. decoupled boundary layers in VOCALS-REx, Atmos. Chem. Phys., 11, 7143–7153, doi:10.5194/acp-11-7143-2011, 2011. 8297, 8299, 8301

Kazil, J., Wang, H., Feingold, G., Clarke, A. D., Snider, J. R., and Bandy, A. R.: Modeling chemical and aerosol processes in the transition from closed to open cells during VOCALS-

REx, Atmos. Chem. Phys., 11, 7491–7514, doi:10.5194/acp-11-7491-2011, 2011. 8290, 8291, 8306, 8310, 8311

Klein, S. A. and Hartmann, D. L.: The seasonal cycle of low stratiform clouds, J. Climate, 6, 1587–1606, doi:10.1175/1520-0442(1993)006<1587:TSCOLS>2.0.CO;2, 1993. 8296

Kollias, P., Fairall, C. W., Zuidema, P., Tomlinson, J., and Wick, G. A.: Observations of marine stratocumulus in SE Pacific during the PACS 2003 cruise, Geophys. Res. Lett., 31, L22110, doi:10.1029/2004GL020751, 2004. 8305

Leon, D. C., Wang, Z., and Liu, D.: Climatology of drizzle in marine boundary layer clouds based on 1 year of data from CloudSat and Cloud-Aerosol Lidar and Infrared Pathfinder Satellite Observations (CALIPSO), J. Geophys. Res., 113, D00A14, doi:10.1029/2008JD009835, 2008. 8295, 8296

Martin, G., Johnson, D., and Spice, A.: The measurement and parameterization of effective radius of droplets in warm stratocumulus clouds, J. Atmos. Sci., 51, 1823–1842, doi:10.1175/1520-0469(1994)051<1823:TMAPOE>2.0.CO;2, 1994. 8293

Mechem, D. B. and Kogan, Y. L.: Simulating the transition from drizzling marine stratocumulus to boundary layer cumulus with a mesoscale model, Mon. Weather Rev., 131, 2342–2360, 2003. 8290

Mechoso, C. R., Wood, R., Weller, R., Bretherton, C. S., Clarke, A. D., Coe, H., Fairall, C., Farrar, J. T., Feingold, G., Garreaud, R., Grados, C., McWilliams, J., de Szoeke, S. P., Yuter, S. E., and Zuidema, P.: Ocean–cloud–atmosphere–land interactions in the southeastern Pacific: the VOCALS program, B. Am. Meteorol. Soc., doi:10.1175/BAMS-D-11-00246.1, in press, 2014. 8291

Muhlbauer, A., McCoy, I. L., and Wood, R.: Climatology of stratocumulus cloud morphologies: microphysical properties and radiative effects, Atmos. Chem. Phys. Discuss., 14, 6981–7023, doi:10.5194/acpd-14-6981-2014, 2014. 8301

Petters, M. D., Snider, J. R., Stevens, B., Vali, G., Faloona, I., and Russell, L. M.: Accumulation-mode aerosol, pockets of open cells, and particle nucleation in the remote subtropical Pacific marine boundary layer, J. Geophys. Res., 111, D02206, doi:10.1029/2004JD005694, 2006. 8290, 8302, 8305, 8310, 8319, 8321

Saide, P. E., Spak, S. N., Carmichael, G. R., Mena-Carrasco, M. A., Yang, Q., Howell, S., Leon, D. C., Snider, J. R., Bandy, A. R., Collett, J. L., Benedict, K. B., de Szoeke, S. P., Hawkins, L. N., Allen, G., Crawford, I., Crosier, J., and Springston, S. R.: Evaluating WRF-

Chem aerosol indirect effects in Southeast Pacific marine stratocumulus during VOCALS-REx, Atmos. Chem. Phys., 12, 3045–3064, doi:10.5194/acp-12-3045-2012, 2012. 8290
Savic-Jovcic, V. and Stevens, B.: The structure and mesoscale organization of precipitating stratocumulus, J. Atmos. Sci., 65, 1587–1605, doi:10.1175/2007JAS2456.1, 2008. 8299
Sharon, T. M., Albrecht, B. A., Jonsson, H. H., Minnis, P., Khaiyer, M. M., van Reken, T. M., Seinfeld, J., and Flagan, R.: Aerosol and cloud microphysical characteristics of rifts and gradients in maritime stratocumulus clouds, J. Atmos. Sci., 63, 983–997, doi:10.1175/JAS3667.1, 2006. 8290, 8298, 8302, 8305, 8310, 8319, 8321
Stevens, B., Vali, G., Comstock, K., Wood, R., Van Zanten, M. C., Austin, P. H., Bretherton, C. S., and Lenschow, D. H.: Pockets of open cells and drizzle in marine stratocumulus, B. Am. Meteorol. Soc., 86, 51–57, doi:10.1175/BAMS-86-1-51, 2005. 8289, 8290, 8296, 8297
Terai, C. R. and Wood, R.: Aircraft observations of cold pools under marine stratocumulus, Atmos. Chem. Phys., 13, 9899–9914, doi:10.5194/acp-13-9899-2013, 2013. 8299, 8301
Terai, C. R., Wood, R., Leon, D. C., and Zuidema, P.: Does precipitation susceptibility vary with increasing cloud thickness in marine stratocumulus?, Atmos. Chem. Phys., 12, 4567–4583, doi:10.5194/acp-12-4567-2012, 2012. 8293
Tomlinson, J. M., Li, R., and Collins, D. R.: Physical and chemical properties of the aerosol within the southeastern Pacific marine boundary layer, J. Geophys. Res., 112, D12211, doi:10.1029/2006JD007771, 2007. 8305
Turton, J. D. and Nicholls, S.: A study of the diurnal variation of stratocumulus using a multiple mixed layer model, Q. J. Roy. Meteor. Soc., 113, 969–1009, doi:10.1002/qj.49711347712, 1987. 8299
Toniazzo, T., Abel, S. J., Wood, R., Mechoso, C. R., Allen, G., and Shaffrey, L. C.: Large-scale and synoptic meteorology in the south-east Pacific during the observations campaign VOCALS-REx in austral Spring 2008, Atmos. Chem. Phys., 11, 4977–5009, doi:10.5194/acp-11-4977-2011, 2011. 8290, 8295, 8296
Van Zanten, M. C. and Stevens, B.: Observations of the structure of heavily precipitating marine stratocumulus, J. Atmos. Sci., 62, 4327–4342, 2005. 8291, 8298, 8302, 8319, 8320, 8321
Wang, H. and Feingold, G.: Modeling mesoscale cellular structure and drizzle in marine stratocumulus, Part I: Impact of drizzle on the formation and evolution of open cells, J. Atmos. Sci., 66, 3237–3256, doi:10.1175/2009JAS3022.1, 2009a. 8290, 8291
Wang, H. and Feingold, G.: Modeling mesoscale cellular structure and drizzle in marine stratocumulus, Part II: The microphysics and dynamics of the boundary region between open

ACPD
14, 8287–8332, 2014

and closed cells, J. Atmos. Sci., 66, 3257–3275, doi:10.1175/2009JAS3120.1, 2009b. 8290, 8291

Wang, H., Feingold, G., Wood, R., and Kazil, J.: Modelling microphysical and meteorological controls on precipitation and cloud cellular structures in Southeast Pacific stratocumulus, Atmos. Chem. Phys., 10, 6347–6362, doi:10.5194/acp-10-6347-2010, 2010. 8290, 8291, 8299, 8311

Wood, R. and Hartmann, D. L.: Spatial variability of liquid water path in marine low cloud: the importance of mesoscale cellular convection. J. Climate, 19, 1748–1764, doi:10.1175/JCLI3702.1, 2006. 8289

Wood, R., Comstock, K. K., Bretherton, C. S., Cornish, C., Tomlinson, J., Collins, D. R., and Fairall, C.: Open cellular structure in marine stratocumulus sheets, J. Geophys. Res., 113, D12207, doi:10.1029/2007JD009596, 2008. 8289, 8290, 8295, 8296, 8305, 8310, 8311, 8321

Wood, R., Bretherton, C. S., Leon, D., Clarke, A. D., Zuidema, P., Allen, G., and Coe, H.: An aircraft case study of the spatial transition from closed to open mesoscale cellular convection over the Southeast Pacific, Atmos. Chem. Phys., 11, 2341–2370, doi:10.5194/acp-11-2341-2011, 2011a. 8289, 8290, 8291, 8294, 8297, 8299, 8300, 8302, 8303, 8305, 8307, 8324

Wood, R., Mechoso, C. R., Bretherton, C. S., Weller, R. A., Huebert, B., Straneo, F., Albrecht, B. A., Coe, H., Allen, G., Vaughan, G., Daum, P., Fairall, C., Chand, D., Gallardo Klenner, L., Garreaud, R., Grados, C., Covert, D. S., Bates, T. S., Krejci, R., Russell, L. M., de Szoeke, S., Brewer, A., Yuter, S. E., Springston, S. R., Chaigneau, A., Toniazzo, T., Minnis, P., Palikonda, R., Abel, S. J., Brown, W. O. J., Williams, S., Fochesatto, J., Brioude, J., and Bower, K. N.: The VAMOS Ocean-Cloud-Atmosphere-Land Study Regional Experiment (VOCALS-REx): goals, platforms, and field operations, Atmos. Chem. Phys., 11, 627–654, doi:10.5194/acp-11-627-2011, 2011b. 8291, 8292, 8293, 8294

Yang, M., Blomquist, B. W., and Huebert, B. J.: Constraining the concentration of the hydroxyl radical in a stratocumulus-topped marine boundary layer from sea-to-air eddy covariance flux measurements of dimethylsulfide, Atmos. Chem. Phys., 9, 9225–9236, doi:10.5194/acp-9-9225-2009, 2009.

Yang, Q., Gustafson Jr., W. I., Fast, J. D., Wang, H., Easter, R. C., Morrison, H., Lee, Y.-N., Chapman, E. G., Spak, S. N., and Mena-Carrasco, M. A.: Assessing regional scale predictions of aerosols, marine stratocumulus, and their interactions during VOCALS-REx us-

ing WRF-Chem, Atmos. Chem. Phys., 11, 11951–11975, doi:10.5194/acp-11-11951-2011, 2011. 8290

Zuidema, P., Leon, D., Pazmany, A., and Cadeddu, M.: Aircraft millimeter-wave passive sensing of cloud liquid water and water vapor during VOCALS-REx, Atmos. Chem. Phys., 12, 355–369, doi:10.5194/acp-12-355-2012, 2012. 8293

ACPD

14, 8287–8332, 2014

Table 1. Time and location of POC flights. The local standard time is UTC − 5.3 h at 80° W. Location denotes the center of the all flight legs flown for POC sampling.

Flight	Date	Time sampled - UTC	Location sampled
RF06	28 Oct 2008	08:24–13:23	18° S 80° W
RF07	31 Oct 2008	08:32–11:37	22.5° S 80° W
RF08	2 Nov 2008	09:07–12:24	22.5° S 80° W
RF09	4 Nov 2008	08:39–11:32	22° S 80° W
RF13	13 Nov 2008	16:03–20:11	19.5° S 78° W

ACPD
14, 8287–8332, 2014

Table 2. Boundary layer and free tropospheric conditions in the POC and overcast (OVC) regions of the five observed POC cases. In addition to the five VOCALS cases examined in this study, the mean conditions at 80° W during the VOCALS field campaign and measurements reported in previous studies are listed for comparison. Mean and standard deviations are recorded as $\mu \pm \sigma$, whereas 25th–75th percentile ranges are shown as a range $x_{25th} - x_{75th}$. For conditions that vary with height level, the variables are preceded by SC (subcloud), CL (cloud), and AC (above cloud) to indicate the height level at which the measurements were taken. The inversion base height ($z_{i,\,base}$) is estimated from the profile legs as the height of the coldest temperature in the lower troposphere. The inversion height (z_i) is estimated from the profile legs as the height of the maximum of the 5 s-running-mean of $d\theta/dz$. The lower-tropospheric stability (LTS), defined as the potential temperature difference between 700 hPa and the surface, was calculated from taking the difference between the mean SC leg potential temperature and the mean potential temperatures calculated by the C-130 between 699 and 701 hPa and within ± 2.5° latitude and longitude of the POC location in Table 1.

Case	Region	$z_{i,\,base}$ (m)	z_i (m)	LTS (K)	AC q_v (g kg^{-1})	SST (°C)	T_0 − SST (K)	SC U (m s^{-1})
RF06	POC	1262 ± 74	1411 ± 22	27	0.53 ± 0.21	17.3	−1.0	11.3 ± 0.9
	OVC	1338 ± 49	1393 ± 18	26	0.21 ± 0.03	17.7	−0.5	11.1 ± 0.9
RF07	POC	1587 ± 15	1658 ± 25	22	0.27 ± 0.03	17.3	−1.6	8.0 ± 1.4
	OVC	1613 ± 41	1654 ± 23	21	0.23 ± 0.07	17.7	−1.0	9.7 ± 1.1
RF08	POC	1599 ± 92	1642 ± 113	23	0.31 ± 0.05	17.5	−0.6	7.7 ± 1.1
	OVC	1656 ± 34	1672 ± 24	23	0.24 ± 0.06	17.6	−0.0	8.2 ± 0.7
RF09	POC	1420 ± 58	1543 ± 129	24	0.26 ± 0.12	17.5	−1.5	7.2 ± 1.1
	OVC	1521 ± 107	1539 ± 101	23	0.68 ± 0.10	17.8	−0.8	5.7 ± 0.7
RF13	POC	1343 ± 31	1365 ± 16	30	0.78 ± 0.12	17.9	−1.7	4.9 ± 1.2
	OVC	1298 ± 15	1307 ± 19	29	0.33 ± 0.09	17.5	−0.3	5.0 ± 1.2
Mean 20S 80W		1220–1330[a]		24.7 ± 2.4[b]		17.8 ± 0.4[a]		8.0 ± 1.9[b]
DYCOMS II								
VS05[c]	POC	794						
	OVC	794						
P06[d]	POC	794						
DECS								
S06[e]	POC	740–800						
	OVC	710 ± 75						

[a] Inferred from Bretherton et al. (2010).
[b] Estimated from flight-mean C-130 data taken between 77.5 and 82.5° W across eleven research flights.
[c] Van Zanten and Stevens (2005).
[d] Petters et al. (2006).
[e] Sharon et al. (2006).

ACPD
14, 8287–8332, 2014

Table 3. Similar to Table 2 but for boundary layer thermodynamic and cloud macrophysical properties. The lifting condensation levels (LCL) from the SC legs are reported here. Cloud fraction (CF) is based on the WCL cloud detection from the subcloud legs. The decoupling parameter Δz is the mean height difference between the cloud base height and the LCL.

Case	Region	Δz (m)	LCL (m)	CL $\overline{w'^2}$ ($m^2 s^{-2}$)	CF (%)	SC LWP ($g m^{-2}$)	$Z_{max}R$ ($mm d^{-1}$)
RF06	POC	343	480	0.17	56	251 ± 238	4.3
	OVC	89	829	0.69	100	173 ± 86	2.6
RF07	POC	781	605	0.05	75	27 ± 25	5.8
	OVC	255	950	0.52	100	166 ± 79	2.1
RF08	POC	545	619	0.09	80	110 ± 81	5.0
	OVC	299	968	0.67	100	131 ± 107	0.6
RF09	POC	429	532	0.08	73	107 ± 194	1.7
	OVC	–	845	0.37	–	137 ± 62	1.3
RF13	POC	372	419	0.03	83	215 ± 206	2.8
	OVC	517	569	0.12	100	59 ± 39	0.3
Mean 20° S 80° W		309 ± 147[a]	840 ± 60[b]	0.53 ± 0.14[a]	90 ± 4[b]	81 ± 10[b]	0.3–2.3[a]
DYCOMS II VS05[c]	POC			0.42 ± 0.03			
	OVC			0.32 ± 0.03			

[a] Estimated from flight-mean C-130 data taken between 77.5 and 82.5° W across eleven research flights.
[b] Inferred from de Szoeke et al. (2012).
[c] Van Zanten and Stevens (2005).

ACPD
14, 8287–8332, 2014

Table 4. Similar to Table 2 but for cloud microphysical and aerosol properties. Aerosol concentrations are filtered for possible drizzle shattering events.

Case	Region	N_d (cm^{-3})	CL q_c ($g\,kg^{-1}$)	CL q_D ($g\,kg^{-1}$)	SC N_a (cm^{-3})	CL N_a (cm^{-3})	SC CN (cm^{-3})	CL CN (cm^{-3})
RF06	POC	10 ± 13	0.06	0.11	32 ± 18	1.7 ± 4.7	137	80
	OVC	94 ± 21	0.31	0.03	103 ± 25	–	145	–
RF07	POC	4 ± 3	0.03	0.08	29 ± 9	1.1 ± 1.8	140	80
	OVC	67 ± 29	0.34	0.04	74 ± 20	–	195	–
RF08	POC	13 ± 12	0.06	0.09	40 ± 13	22.0 ± 11.4	383	261
	OVC	208 ± 75	0.27	0.00	324 ± 166	–	636	–
RF09	POC	6 ± 11	0.02	0.05	24 ± 12	6.1 ± 12.2	307	214
	OVC	52 ± 20	0.14	0.02	65 ± 9	–	207	–
RF13	POC	8 ± 8	0.04	0.06	37 ± 11	4.2 ± 3.9	177	316
	OVC	94 ± 62	0.26	0.02	90 ± 13	–	247	–
Mean 20° S 80° W		133 ± 57[a]	0.09–0.29[a]	0.00–0.04[a]	70–220[b]	–	300–480[b]	–
DYCOMS II								
VS05[c]	POC	55 ± 16						
	OVC	70 ± 17						
P06[d]	POC	30 ± 15			40			
DECS								
S06[e]	POC	20			~ 10			
	OVC	40–60			~ 50			
W08[f]	POC				~ 20–50			
	OVC				~ 100–300			

[a] Estimated from leg-mean C-130 data taken between 77.5 and 82.5° W across eleven research flights.
[b] Inferred from Allen et al. (2011).
[c] Van Zanten and Stevens (2005).
[d] Petters et al. (2006).
[e] Sharon et al. (2006).
[f] Wood et al. (2008)

ACPD
14, 8287–8332, 2014

Table 5. In situ measurements of cloud and drizzle properties of active and quiescent clouds observed across the five POC cases. A $\overline{w'^2}$ threshold of 0.1 $m^2 s^{-2}$ is used to categorize cloud measurements as either active or quiescent, except for the day-time flight RF13, where a threshold of 0.03 $m^2 s^{-2}$ is used. All active and quiescent values are averaged over in-cloud measurements, defined as measurements for which the combined liquid water mixing ratio from CDP and 2DC is greater than 0.03 $g kg^{-1}$ or the PVM liquid water content is greater than 0.03 $g kg^{-1}$.

Case	Cloud	Length (km)	Fraction (%)	$\overline{w'^2}$ ($m^2 s^{-2}$)	N_d (cm^{-3})	N_D (L^{-1})	q_c ($g kg^{-1}$)	q_D ($g kg^{-1}$)	R_{insitu} ($mm d^{-1}$)
RF06	Active	32.5	14.6	0.70	21	280	0.29	0.22	24.0
	Quiescent	78.2	35.1	0.03	5	272	0.05	0.22	15.1
RF07	Active	2.0	3.3	0.17	5	233	0.07	0.09	3.5
	Quiescent	24.4	40.6	0.04	5	323	0.06	0.19	9.3
RF08	Active	14.6	22.5	0.18	19	213	0.12	0.15	11.5
	Quiescent	23.6	36.3	0.05	9	274	0.08	0.16	7.9
RF09	Active	5.2	4.3	0.55	26	49	0.15	0.02	2.1
	Quiescent	37.4	31.2	0.03	3	188	0.03	0.15	8.6
RF13	Active	32.0	15.1	0.06	15	214	0.16	0.11	5.9
	Quiescent	52.5	24.8	0.01	4	307	0.06	0.16	9.9

ACPD
14, 8287–8332, 2014

Table 6. Aerosol budget values. Values relevant to the aerosol budget of Eq. (1) are listed. Measured values include, PCASP-sized aerosols from subcloud (N_s) and below cloud (N_+) flight legs and Δq, the mean difference in water (vapor + cloud) mixing ratio between cloudy and clear conditions measured in below cloud legs. The surface aerosol flux (F) of PCASP-sized aerosols is estimated from the subcloud leg-mean wind speed (see Table 2) using the parameterization from Clarke et al. (2006). POC-mean precipitation rate (R_{500}) at 500 m is estimated from the radar reflectivity at 500 m using the Z–R relationship proposed by Comstock et al. (2004) (R (mm d^{-1}) = 2.01 $Z^{0.77}$). The cumulus mass flux M_{Cu} is estimated using the relationship in Eq. (2).

Case	N_s (cm^{-3})	N_+ (cm^{-3})	$N_s - N_+$ (cm^{-3})	F ($\times 10^3$ m^2 s^{-2})	R_{500} (mm d^{-1})	Δq (g kg^{-1})	M_{Cu} (cm s^{-1})	F/M_{Cu} cm^{-3})
RF06	32	16	16	230	2.2	0.9	2.8	8.1
RF07	29	18	11	70	2.8	1.2	2.7	2.6
RF08	40	23	17	62	2.7	1.1	2.8	2.2
RF09	24	20	4	49	0.8	0.9	1.0	4.8
RF13	37	12	15	13	1.5	0.8	2.2	0.6

ACPD
14, 8287–8332, 2014

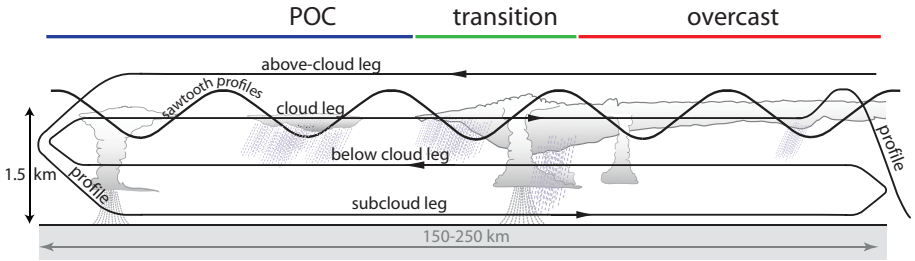

Fig. 1. Typical flight strategy taken by the NSF/NCAR C-130 during POC sampling (adapted from Fig. 7 of Wood et al., 2011a).

ACPD
14, 8287–8332, 2014

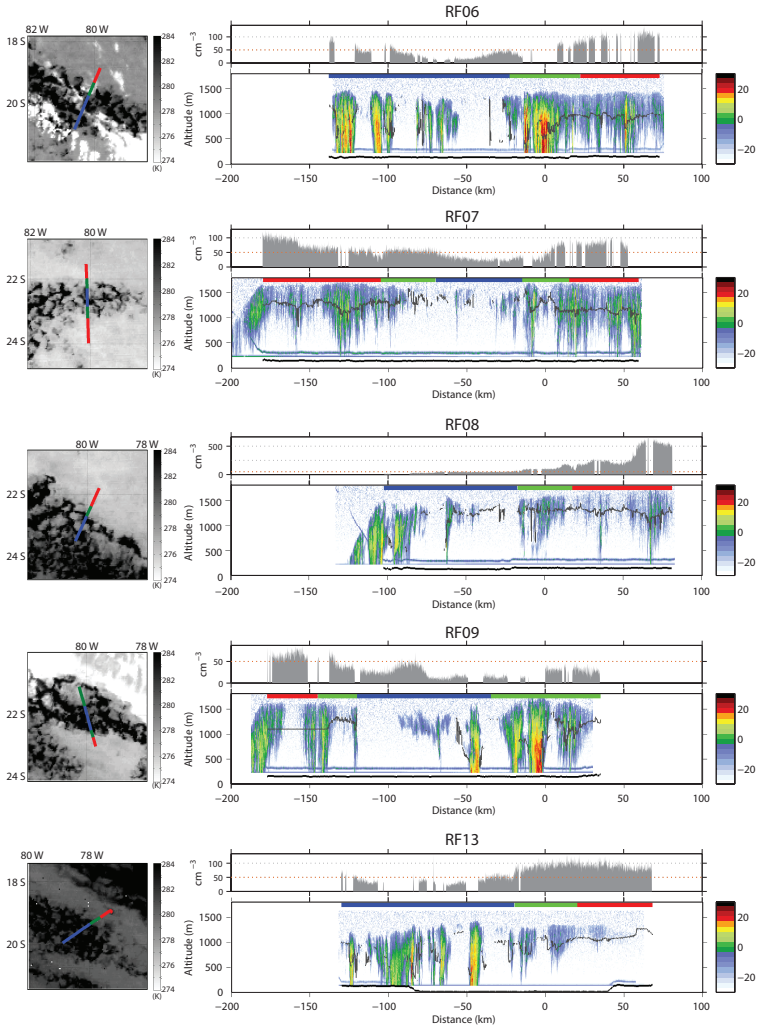

ACPD
14, 8287–8332, 2014

Aircraft observations of five POCs

C. R. Terai et al.

CC BY

Fig. 2. C-130 flight tracks overlaid on GOES-10 satellite imagery, in situ PCASP concentrations, and Wyoming Cloud Radar (WCR) reflectivity cross-sections from subcloud legs of the five POC cases analyzed in this study. For each POC case, the left panel shows the location of the flight legs in relation to the overall POC structure. The flight track is colored by distinction between POC (blue), overcast (red), and transition (green). The top panel for each case shows the aerosol concentration as measured by the PCASP ($0.1\,\mu m < D < 3\,\mu m$), where concentrations are filtered for drizzle events. The dotted line indicating $50\,cm^{-3}$ is highlighted in orange to remind the reader of the changing scale along the ordinate. The panel below the PCASP concentrations shows the WCR column reflectivities with the cloud base height from Wyoming Cloud Lidar traced in gray. All radar cross-sections and aerosol concentration time series are aligned along the middle of the north transition region.

ACPD
14, 8287–8332, 2014

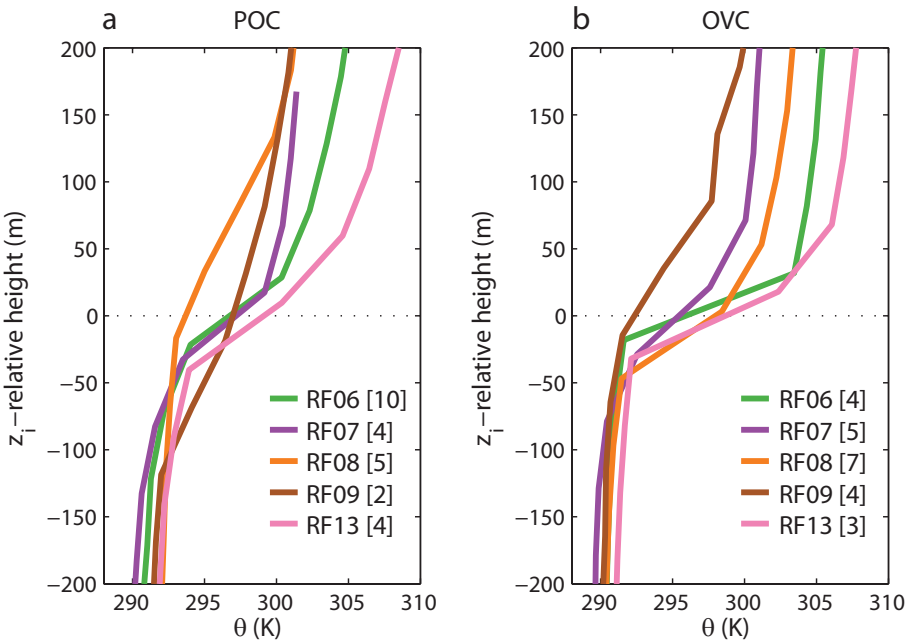

Fig. 3. Potential temperature (θ) structure in POCs (left) and in overcast regions (right). Profiles are mean profiles based on data from profiles binned every 25 m. The mean height of maximum potential temperature increase is subtracted from each profile to examine the structures relative to the inversion height. Instead of the inversion base height, the mean height of the maximum vertical gradient in potential temperature so that the temperature changes in each area are more aligned.

ACPD
14, 8287–8332, 2014

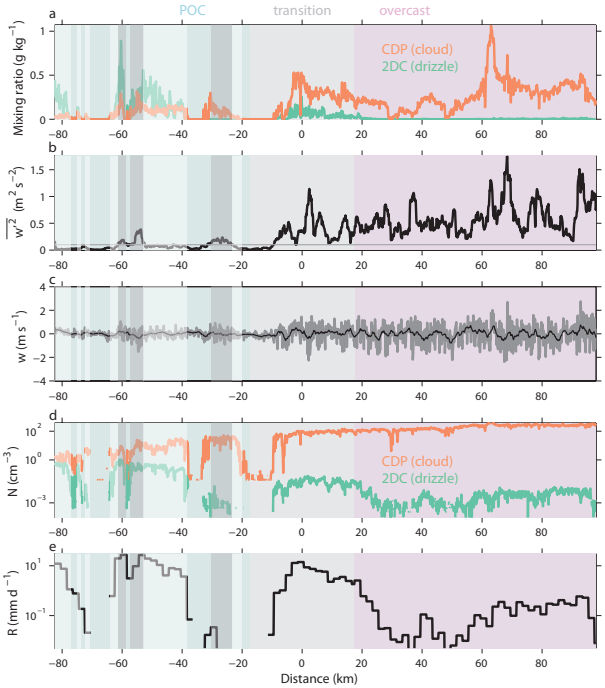

Fig. 4. Cloud level measurements from cloud level flight leg showing **(a)** cloud (q_c – orange) and drizzle (q_D – green) water mixing ratio; **(b)** 21 s running vertical wind variance ($\overline{w'^2}$); **(c)** 1 Hz vertical wind speed (w – gray) and 21 s mean w (black); **(d)** cloud (orange – N_d) and drizzle (green – N_D) drop number concentration; and **(e)** precipitation rate R, based on 10 s averaged drizzle drop size distributions. In the POC segment of the flight leg, active clouds, defined as cloudy and drizzling data with $\overline{w'^2} \geq 0.1\,\mathrm{m^2\,s^{-2}}$, are shaded in dark gray. Quiescent clouds, defined as cloudy and drizzling data with $\overline{w'^2} < 0.1\,\mathrm{m^2\,s^{-2}}$, are shaded in white. The clear regions in the POC, where liquid water mixing ratios measured by the CDP or the PVM did not exceed 0.03 g kg^{-1}, are left unshaded.

ACPD
14, 8287–8332, 2014

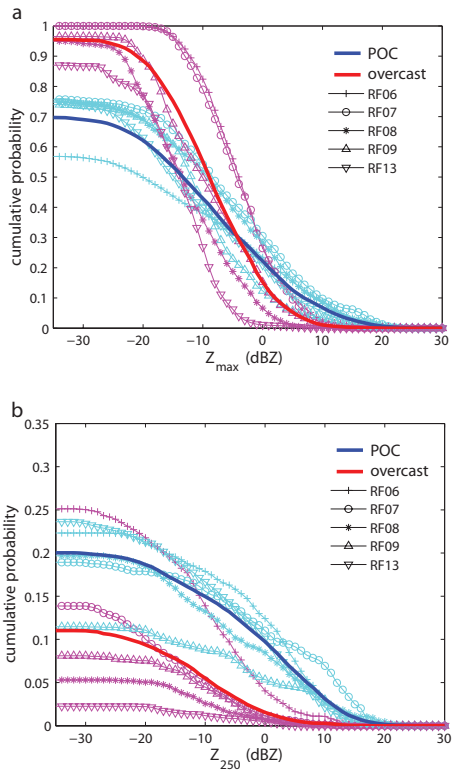

Fig. 5. (a) The cumulative probability of column maximum radar reflectivity Z_{max} greater than the abscissal value for overcast (red) and POC (blue) regions. The mean distribution are shown as bold lines, while individual flight legs are shown as thinner lines with markers. Radar reflectivities from all level flight legs are used to make the distribution. **(b)** Same as Fig. 5a, but for radar reflectivity at 250 m.

ACPD
14, 8287–8332, 2014

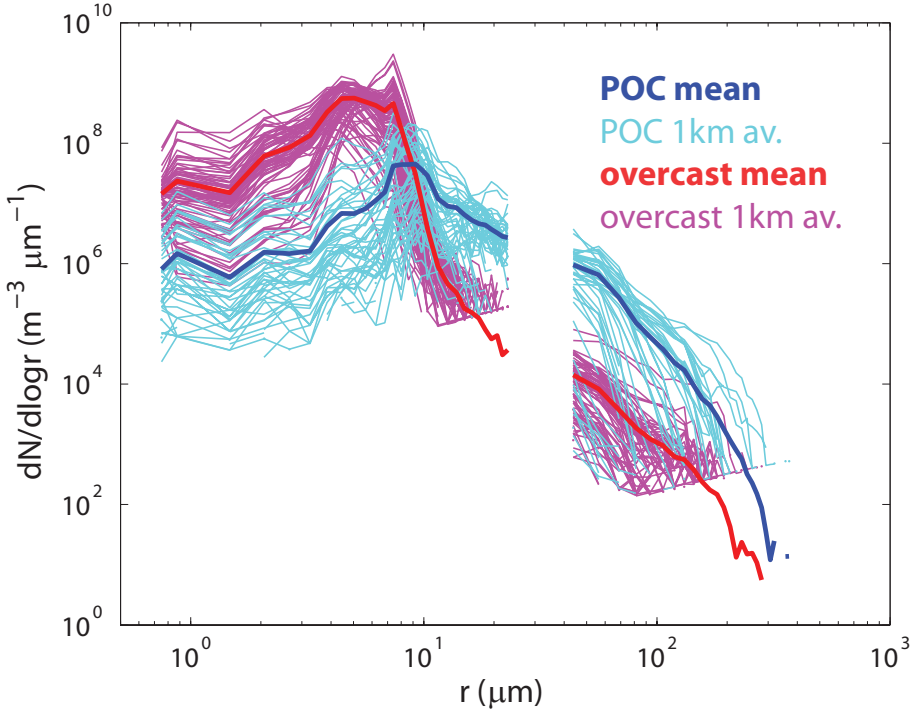

Fig. 6. Droplet size distribution from the CDP and 2DC during a cloud-level flight leg from RF08. The cyan lines indicate distributions estimated from 1 km averages in the POC, while the heavier blue line indicates the mean of those distributions. The magenta lines indicate distributions estimated from 1 km averages in the overcast region, while the heavier red line indicates the mean of those distributions.

ACPD
14, 8287–8332, 2014

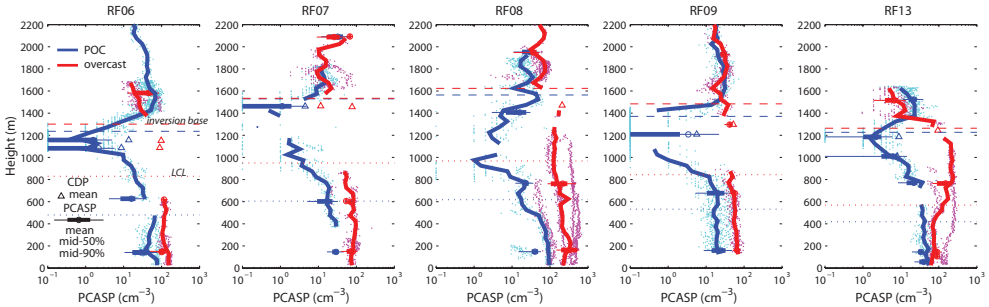

Fig. 7. Profiles of PCASP aerosol concentration from the POC (blue) and overcast (red) region. Cyan (POC) and magenta (overcast) dots indicate individual data points from profiles flown in the two regions. Concentrations $< 0.1\,\mathrm{cm}^{-3}$ are set at $0.1\,\mathrm{cm}^{-3}$ to allow for easier plotting on the log-scale abscissa. Heavier profile line indicates the median taken from the profile data. PCASP data from level flight legs are also included in the form of whisker plots. For reference, cloud-mean cloud droplet number concentrations from the CDP are shown as open triangles, mean inversion base heights calculated from profile measurements are shown as dashed lines, and mean lifting condensation levels calculated from subcloud flight legs are shown as dotted lines.

ACPD
14, 8287–8332, 2014

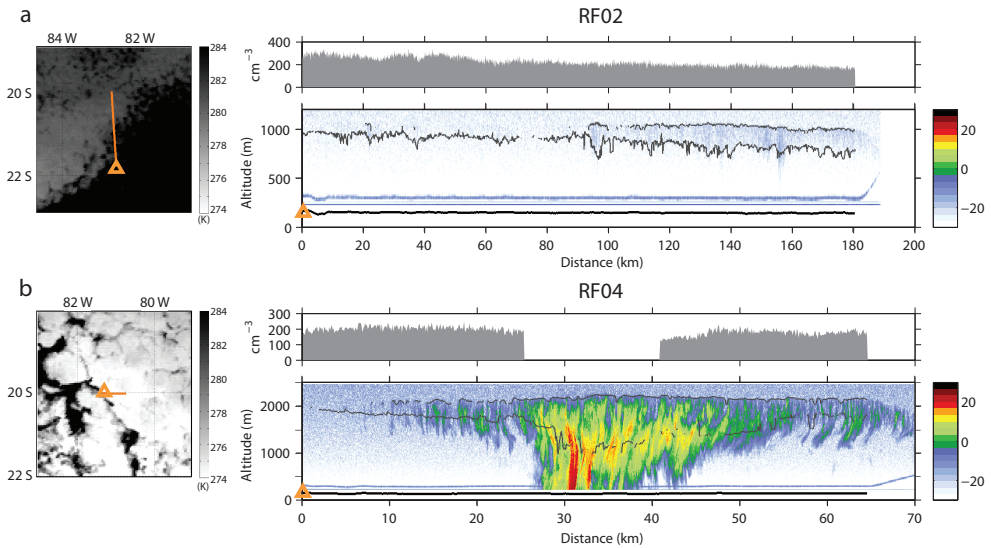

Fig. 8. (a) C-130 subcloud flight track from RF02 (18 October 2008 16:50 UTC) is overlaid on GOES-10 infrared satellite imagery taken at same time. As in Fig. 2, the top right panel shows the in situ PCASP aerosol concentrations at ~ 150 m. The bottom right panel shows the WCR reflectivity with the flight altitude indicated in bold black and the WCR/WCL-derived cloud top height and cloud base height indicated in gray. **(b)** Same as **(a)** but for a subcloud flight track from RF04 (23 October 2008 10:20 UTC).

ACPD
14, 8287–8332, 2014